COMPUTER VISION AND IMAGE UNDERSTANDING
Vol. 66, No. 2, May, pp. 207–222, 1997
ARTICLE NO. IV970605

# Spatial Transformation and Registration of Brain Images Using Elastically Deformable Models

Christos Davatzikos

*Division of Neuroradiology, Department of Radiology and Radiological Science, The Johns Hopkins University School of Medicine, 600 N. Wolfe Street, Baltimore, Maryland 21287*

Received August 13, 1996; accepted December 13, 1996

**The development of algorithms for the spatial transformation and registration of tomographic brain images is a key issue in several clinical and basic science medical applications, including computer-aided neurosurgery, functional image analysis, and morphometrics. This paper describes a technique for the spatial transformation of brain images, which is based on elastically deformable models. A deformable surface algorithm is used to find a parametric representation of the outer cortical surface and then to define a map between corresponding cortical regions in two brain images. Based on the resulting map, a three-dimensional elastic warping transformation is then determined, which brings two images into register. This transformation models images as inhomogeneous elastic objects which are deformed into registration with each other by external force fields. The elastic properties of the images can vary from one region to the other, allowing more variable brain regions, such as the ventricles, to deform more freely than less variable ones. Finally, the framework of prestrained elasticity is used to model structural irregularities, and in particular the ventricular expansion occurring with aging or diseases, and the growth of tumors. Performance measurements are obtained using magnetic resonance images.** 

## I. INTRODUCTION

A key issue in several medical applications that involve the analysis of brain images is morphological variability. Specifically, the shape of the brain varies considerably from one person to another, rendering the comparison, analysis, and summarization of data from different individuals a very difficult task. The purpose of a spatial or geometric transformation of brain images is to reduce the effects of such inter-individual differences in the shape of the brain, thereby improving the accuracy of the analysis of superimposed images from different individuals.

The spatial transformation of images plays an important role in image guided neurosurgery, since it allows the accurate superposition of anatomical atlases over patient data, thereby assisting in the planning and performance of a surgical procedure. In particular, certain structures, such as the optic nerve and radiations, the thalamic nuclei, and the Brodman cytoarchitectonic areas of the cortex, are not visible even in high-resolution magnetic resonance images. Such structures are outlined in detail in various brain atlases. However, in order to be utilized in a surgical procedure, they must be mapped to the brain morphology of the individual patient. This is accomplished by a spatial transformation which brings the atlas and the patient's image *into register,* i.e., into spatial coincidence.

The spatial transformation of images is also important in functional [1, 2] stereotaxis, in which brain regions that are activated during certain tasks are typically identified through a statistical analysis of data from a large number of subjects [1]. Prior to this analysis, the images from all subjects must be mapped to a canonical reference system, in which they are in register, i.e., homologous regions have the same coordinates. This is accomplished through a spatial transformation that matches individual images with a template which is defined in this conanical coordinate system.

Finally, the spatial transformation of images is important in structural stereotaxis [3–6], in which morphological differences between two brains are precisely quantified using the transformation that maps one brain image to the other. Certain properties of this transformation can be used to study morphological brain differences that are due to sex, age, diseases, or other factors.

Several methodologies for the spatial transformation of brain images have been proposed in the literature. In [6, 7] a number of landmarks in two images to be registered is defined manually, and a spline transformation matching these landmarks is used to register the images. Transformation techniques based on maximizing similarity measures have been developed by the groups in the University of Pennsylvania [8–10], Washington University [11, 12], and Montreal Neurological Institute [13]. Other approaches are based on polynomial or Fourier transformations [14, 15]. Also related is the work in [5] which uses a sequence of increasingly localized transformations to register



1077-3142/97 $25.00

the surface of the skull, and the work in [16] which uses the concept of deamons which attempt to maximize the overlap of the ''interior'' and the ''exterior'' of a brain structure of interest in one image with their counterparts in another.

Related is also the literature on motion estimation [17–22], in which the problem is finding a transformation between two consecutive frames rather than between two different brain images. There are two fundamental differences, however, between these two problems. The first is that in motion estimation the deformation between consecutive frames is very small. Therefore, corresponding features are typically found through a local search around the configuration of the deforming object at each particular instance. The second difference is that in motion tracking, the same object is observed in both images. Therefore, features used to determine the deformation field are expected to be very similar.

The approach described in this paper is based on elastically deformable models with inhomogeneous elastic properties. Specifically, a deformable surface algorithm is first used to obtain a parametric representation of the outer surface of the cortex. Based on this representation, geometric features of the cortical surface, such as various curvatures, are determined and used for the identification and matching of sulci, gyri, fissures, and other distinct cortical characteristics. Resulting from this procedure is a one-to-one map between the three-dimensional images of two individuals, which corresponds major anatomical features in one image with their homologues in another. This map is subsequently used to obtain a 3D warping of one image into registration with the other, by solving the equations governing the deformation of an inhomogeneous elastic object. In order to model structural irregularities, such as ventricular expansion and tumor growth, we propose the framework of prestrained elasticity. In this framework, the brain is originally assumed to be in a strained configuration. As this strained condition is relaxed, it results in the expansion or contraction of certain structures within which a strain energy was initially distributed uniformly.

## II. SPATIAL TRANSFORMATION ALGORITHM FOR REGISTRATION (STAR)

### II.A. *Overview*

Elastic deformation transformations have several features which make them suitable to the problem of brain image registration. Most importantly, they are smooth transformations which tend to preserve the relative positions of anatomical structures, while offering a high flexibility to allow for considerable intersubject variability. The transformation methodology described herein is driven by an external force field defined on a number of distinct anatomical surfaces, which can be either open or closed. In this paper we will use two such surfaces: the outer cortical boundary and the ventricular boundary. In Section IV we discuss the extension of our method to include additional surfaces (see also [23, 30]). In our approach, each of these surfaces in one of two images to be registered is warped toward its configuration in the other image. This surface deformation then drives a three-dimensional elastic warping of the rest of the image.

In section II.B we focus on the outer cortical surface. In order to define the external forces that deform the outer cortical surface in one image to that in another, we first establish a map between the outer cortex in the two images. We do this by first finding a parametric representation of the outer cortex using a deformable surface algorithm and then finding the deformation that brings two outer cortical surfaces into registration. We decompose this deformation into two components. The first is a nearly *homothetic map* consisting of a uniform stretching or shrinking followed by an arbitrary bending; this component accounts for overall shape differences and brings the outer cortex in gross correspondence across subjects. The second component is a nonuniform stretching or shrinking, or more precisely a *reparameterization,* which does not alter the overall outer cortical shape; this component accounts for intersubject variability of the cortical folds and attempts to bring individual features (sulci, gyri, lobes, etc.) into better registration.

### II.B. *Outer Cortical Mapping*

Our deformable surface algorithm, which finds a map between the outer cortical surfaces in two images, is described below. A more detailed description of the algorithm can be found in [24, 25].

II.B.1. *Deformable Surface Algorithm.* Throughout our development we will assume that the tomographic magnetic resonance images have been preprocessed. Resulting from this preprocessing ia a *mass function* $m(\mathbf{x}) \in [0, 1]$, which has high value on the boundary of a structure of interest. In the experiments herein we use a binary mass function, which is determined via a threshold-based seeded region growing, in conjunction with an erosion and a conditional dilation which extract the brain tissue and strip off tissues which are not of interest (e.g., skull, skin, fat, etc). The region growing is initialized in the interior of a structure of interest (e.g., parenchyma, ventricles, etc.) and terminates on the boundary of the structure where the mass $m(\cdot)$ is set equal to unity.

Having described the mass function, we now turn our attention to the deformable surface. It is a closed surface, denoted $\mathbf{x}(u, v) = (x(u, v), y(u, v), z(u, v))$, where as customary in the differential geometry literature [26] the

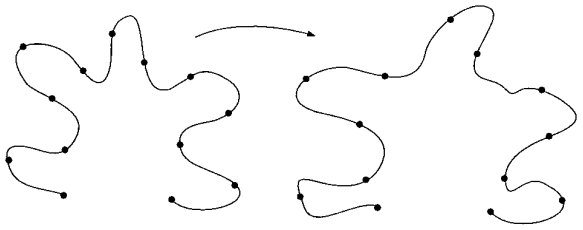

**FIG. 1.** A homothetic deformation consists of a uniform stretching or shrinking followed by an arbitrary bending.

variables $u$ and $v$ are defined on a planar domain $\mathcal{D}$. The deformable surface is initialized at a spherical configuration surrounding the cortex and shrinks like an elastic balloon wrapping around the cortex, being attracted by the outer cortical mass described above. In its final configuration, the deformable surface provides a parametric description of the outer cortical surface which will be used in the following sections.

II.B.2. *Overall Shape Matching.* Consider two volumetric images to be registered, referred to as $\mathcal{V}_1$ and $\mathcal{V}_2$. By applying the deformable surface algorithm to each image separately we obtain a parameterization of the outer cortex in the two images, denoted $\mathbf{x}_1(u, v)$ and $\mathbf{x}_2(u, v)$, respectively. Based on these parametric representations, we next determine a deformation of the outer cortical surface in $\mathcal{V}_1$ which maps it on that in $\mathcal{V}_2$ in a way that anatomically corresponding regions are mapped to each other. We decompose this deformation into two components: the first is described in this section and the second is described in Section II.B.3. The first component is a nearly homothetic map between the two outer cortical surfaces (i.e., an isometry together with a global scaling). This map consists of a uniform stretching or shrinking of the outer cortex in $\mathcal{V}_1$ followed by an arbitrary bending which changes its overall shape. This component matches the overall shape of the brains in $\mathcal{V}_1$ and $\mathcal{V}_2$, but it does not match individual features such as sulci and gyri.

A 2D analog of a homothetic deformation is shown in Fig. 1. In this example, a uniform stretching followed by an arbitrary bending was applied to the left curve in Fig. 1 and deformed it to the right curve in Fig. 1. If a number of points, $p_1, p_2, \ldots, p_N$, are evenly spaced along the left curve in Fig. 1, and an equal number of points, $q_1, q_2, \ldots, q_N$, are evenly spaced along the right curve in Fig. 1, then a map corresponding $p_i$, $i = 1, \ldots, N$, to $q_i$, $i = 1, \ldots, N$, is a homothetic map between the two curves. Analogously in 3D, if a regular grid,[1] $p_{ij}, i, j = 1, \ldots, N$, is placed on one surface and a regular grid, $q_{ij}$, $i, j = 1, \ldots, N$, is placed on a second surface, then the map that corresponds $p_{ij}$ to $q_{ij}$ is a homothetic map between the two surfaces (see, for example, Fig. 6).

The motivation behind seeking a homothetic map between the outer cortex in two brain images is that, although different brains have different shapes, their underlying structures are similar, i.e., the relative positions of sulci and gyri with respect to each other are fairly consistent. For example, in Fig. 1 the two curves, which can be viewed as hypothetical cortical folds, have a very similar structure, although the orientations of their folds differ. Therefore, the homothetic map in this case would bring corresponding regions in the two curves into register.

Although a homothetic map between two arbitrary curves always exists, the same is not true for two arbitrary surfaces. In fact, only in very special cases it is possible to define such a map. Therefore, in our algorithm we find a nearly homothetic map between the outer cortical surfaces in two brains using an interative procedure which minimizes metric and angular distortion. At each step of this iterative procedure, each curve of the first family of isoparametric curves ($u$ is fixed) of each surface is reparameterized to form a constant speed curve. The same is subsequently applied to the second family of isoparametric curves ($v$ is fixed) of each surface. Finally, the isoparametric curves of each surface are reoriented to intersect at right angles. This procedure converges fairly fast, typically in less than ten iterations.

Effectively, the iterative procedure described above places a nearly uniform grid along the outer cortical surface in each image. A map from the outer cortex of one brain to the outer cortex in another brain can be then defined as the one corresponding points with the same parametric coordinates:

$$\mathcal{V}_1 \ni \mathbf{x}_1(u, v) \rightarrow \mathbf{x}_2(u, v) \in \mathcal{V}_2, \quad \forall (u, v) \in \mathcal{D}.$$

In the experiments in Section III.A we demonstrate that this map beings images from different subjects into a gross anatomical correspondence. It should be noted, however, that it does not account for interindividual local variations in the relative position of cortical folds. In order to account for interindividual local variations in the relative position of cortical folds. In order to account for this variability, in the following section we describe a procedure which refines this map, by applying a reparameterization of the cortical surface which matches individual cortical features.

II.B.3. *Curvature Matching.* In order to match individual cortical features between the outer cortex in $\mathcal{V}_1$ and the outer cortex in $\mathcal{V}_2$, we use the curvature maps of the cortex at various scales, which provide complementary information about the cortical structure, as was shown in [24, 25]. For example, global features, such as the cortical

[1] A regular grid has points evenly spaced and its horizontal and vertical curves intersect at right angles.

fissures, the temporal lobes, and the occipital poles, can be identified along the outer cortex from the minimum, maximum, and Gaussian curvatures, respectively, at a coarse scale in which the deformable surface is composed of a relatively small number of polygons. Cortical sulci and gyri can be identified from the minimum and maximum curvatures, respectively, at a finer scale, in which the deformable surface is composed of a relatively large number of polygons.

In order to obtain a match between the curvatures of $\mathbf{x}_1(\cdot, \cdot)$ and $\mathbf{x}_2(\cdot, \cdot)$, we seek a *reparameterization,* $\mathbf{r}(u, v)$, of the surface $\mathbf{x}_1(\cdot, \cdot)$ resulting from the nearly homothetic map discussed in the previous section, which brings its geometric structure into better agreement with that of $\mathbf{x}_2(\cdot, \cdot)$. Let $\kappa^M(u, v)$, $\kappa^m(u, v)$, and $\kappa^G(u, v)$ denote the maximum, minimum, and Gaussian curvatures, respectively, defined at each point $(u, v)$ in the parametric domain $\mathscr{D}$. The reparameterization $\mathbf{r}(u, v)$ is a smooth map of the domain $\mathscr{D}$, on which the deformable surface is defined, onto itself (see, for example, Fig. 11c which shows the curvature of a reparameterization of Fig. 11a). We find this reparameterization be elastically deforming $\mathscr{D}$ onto itself, under the influence of an external force field comprised of two components, $\mathbf{f}_1$ and $\mathbf{f}_2$. The first component attempts to maximize the similarity between the curvature patterns of the reparameterized surface $\mathbf{x}_1(\mathbf{r}(u, v))$ and the target surface $\mathbf{x}_2(u, v)$. In order to make this curvature-based matching independent from the actual values of the curvatures, which can vary from one person to another, and dependent only on the curvature patterns, instead of the curvatures themselves we consider the *curvature binary maps,* which are denoted by $b_i^\alpha(u, v)$, $i \in \{1, 2\}$, $\alpha \in \{M, m, G\}$, and are defined as

$$b_i^\alpha(u, v) = \begin{cases} 1, & \kappa_i^\alpha(u, v) > T, \\ 0, & \text{otherwise}, \end{cases} \tag{1}$$

where $T$ is a positive threshold.

The first component, $\mathbf{f}_1$, of the force in this elastic reparameterization attempts to minimize the squared difference between the curvature binary maps, at the coarse scale, of the reparameterized surface $\mathbf{x}_1(\mathbf{r}(u, v))$ and the target surface $\mathbf{x}_2(u, v)$:

$$\iint_{\mathscr{D}} \{[b_1^M(\mathbf{r}(u, v)) - b_2^M(u, v)]^2 + [b_1^m(\mathbf{r}(u, v)) - b_2^m(u, v)]^2 + [b_1^G(\mathbf{r}(u, v)) - b_2^G(u, v)]^2\}\, du\, dv. \tag{2}$$

Accordingly, $\mathbf{f}_1$ is defined as

$$\mathbf{f}_1(u, v) = \mathbf{f}_1^M(u, v) + \mathbf{f}_1^m(u, v) + \mathbf{f}_1^G(u, v), \tag{3}$$

where

$$\mathbf{f}_1^M(u, v) = -\nabla_{\mathbf{r}} b_1^M(\mathbf{r}(u, v))\, [b_1^M(\mathbf{r}(u, v)) - b_2^M(u, v)]$$

$$\mathbf{f}_1^m(u, v) = -\nabla_{\mathbf{r}} b_1^m(\mathbf{r}(u, v))\, [b_1^m(\mathbf{r}(u, v)) - b_2^m(u, v)]$$

$$\mathbf{f}_1^G(u, v) = -\nabla_{\mathbf{r}} b_1^G(\mathbf{r}(u, v))\, [b_1^G(\mathbf{r}(u, v)) - b_2^G(u, v)].$$

The second component, $\mathbf{f}_2$, of the external force field attempts to match fine cortical features, such as sulci and gyri, which are identified using the curvature cortical maps at finer scale, in which the deformable surface is composed of a larger number of polygons. In the experiments herein we use the minimum curvature, which reflects the shape and location of the cortical sulci. In particular, a two-dimensional image of the minimum curvature of the outer cortex is first obtained in the parametric domain $\mathscr{D}$. The location and shape of the sulci are identified on this image since the minimum curvature has high value (see, for example, Fig. 11). Based on the curvature map, a number, $N$, of sulci and fissures are then outlined; this procedure is currently done manually. The outlined curves are subsequently parameterized by constant speed parameterizations [26], or by piece-wise constant speed parameterizations if specific landmarks can be identified along them. Let $\mathbf{s}_1^i(l)$ and $\mathbf{s}_2^i(l)$, $l \in [0, 1]$, $i = 1, \ldots, N$, be the $N$ pairs of the resulting parametric representations of corresponding sulci along the two outer cortical surfaces to be matched. Here, as $l$ sweeps the unit interval, $\mathbf{s}_1^i(l) \in \mathscr{D}$ and $\mathbf{s}_2^i(l) \in \mathscr{D}$ sweep the two corresponding sulcal curves. The force $\mathbf{f}_2$ attempts to minimize the following measure:

$$\sum_{i=1}^{N} \int_0^1 \|\mathbf{r}(\mathbf{s}_1^i(l)) - \mathbf{s}_2^i(l)\|^2\, dl.$$

Effectively, $\mathbf{f}_2$ seeks a reparameterization $\mathbf{r}(u, v)$ of the domain $\mathscr{D}$ that satisfies the $N$ sulcal maps:

$$\mathbf{s}_1^i(l) \xrightarrow{\mathbf{r}} \mathbf{s}_2^i(l), \quad i = 1, \ldots, N, \quad l \in [0, 1].$$

Accordingly, $\mathbf{f}_2$ is defined as

$$\mathbf{f}_2(\mathbf{s}_1^i(l)) = -\sum_{i=1}^{N} [\mathbf{r}(\mathbf{s}_1^i(l)) - \mathbf{s}_2^i(l)] \tag{4}$$

along the $N$ sulci, and zero elsewhere in $\mathscr{D}$.

Having defined the external force fields, $\mathbf{f}_1$ and $\mathbf{f}_2$, we are now in position to write the equations governing the reparameterization of $\mathscr{D}$, i.e., its elastic deformation onto itself (see also [27]):

$$\lambda_r \Delta \mathbf{r}(u, v) + (\lambda_r + \mu_r) \nabla \mathrm{Div} \mathbf{r}(u, v) + \mathbf{f}_1(u, v) + \mathbf{f}_2(u, v) = 0, \tag{5}$$

where $\lambda_r$ and $\mu_r$ are the Lame moduli in this (2D) elastic

deformation[2] and they are constant throughout the domain $\mathscr{D}$. These equations are discretized and solved using successive overrelaxation with Chebyshev acceleration.

Resulting from the procedures described in this and the previous sections is a map, $\chi$, from the outer cortical surface in $\mathscr{V}_1$ to the outer cortical surface in $\mathscr{V}_2$:

$$\chi: \mathscr{V}_1 \ni \mathbf{x}_1(\mathbf{r}(u,v)) \rightarrow \mathbf{x}_2(u,v) \in \mathscr{V}_2, \tag{6}$$

with

$$\mathbf{r}(u,v), (u,v) \in \mathscr{D}.$$

This map will be used in the following section to derive a 3D transformation of $\mathscr{V}_1$ to $\mathscr{V}_2$.

### II.C. *3D Elastic Warping*

*General Framework.* We now describe our spatial transformation procedure which uses the outer cortical map $\chi$, derived as described in the previous section, to obtain a full 3D registration transformation. In this procedure, we first deform the outer cortex $\mathscr{V}_1$ to its corresponding configuration in $\mathscr{V}_2$, as prescribed by $\chi$ in (6). We then let the remaining image warp, following the equations governing the deformation of an elastic body under an external force field. By varying the elasticity properties throughout the images we allow certain structures to deform more freely than others. Moreover, by using a nonzero strain energy at the reference configuration we allow certain structures (e.g., ventricles) to naturally expand or contract. In our current implementation, this initial strain energy is distributed uniformly throughout the ventricles which tend to expand considerably with age or brain diseases.

A spatial transformation is a function $\mathbf{U}(\cdot)$ which maps a point $\mathbf{x}$ in $\mathscr{V}_1$ to a point $\mathbf{U}(\mathbf{x})$ in $\mathscr{V}_2$. Let $q(\mathbf{x})$ be an indicator function being unity on the outer cortex in $\mathscr{V}_1$ and zero everywhere else. Let, also, $\mathbf{g}(\mathbf{x})$ be the point on the outer cortex in $\mathscr{V}_2$ to which a point $\mathbf{x}$ on the outer cortex in $\mathscr{V}_1$ is mapped through $\chi$. In the STAR algorithm we obtain the transformation $\mathbf{U}(\cdot)$ everywhere in $\mathscr{V}_1$ by solving the equations governing the deformation of an inhomogeneous elastic body with nonzero initial strain, which are derived below.

Let $\lambda$ and $\mu$ be the (spatially varying) elasticity parameters (known as the Lame moduli [28]), and let $\mathbf{E}$ denote the strain tensor.[3] In linear elasticity, $\mathbf{E}$ is given by

$$\mathbf{E} = \frac{1}{2}(\nabla\mathbf{u} + \nabla\mathbf{u}^{\mathrm{T}}) + \mathbf{E}_0, \tag{7}$$

where $\mathbf{u} = \mathbf{u}(\mathbf{x}) = \mathbf{U}(\mathbf{x}) - \mathbf{x}$ is the displacement field from the reference configuration to the deformed configurations. The purpose of the reference strain $\mathbf{E}_0$, which is nonzero in the ventricles, is to cause a uniform ventricular expansion of the reference image $\mathscr{V}_1$, and it is explained in detail later in this section. The strain tensor $\mathbf{E}_0$ is precisely given by

$$\mathbf{E}_0 = \varepsilon(\mathbf{x})\mathbf{I}, \tag{8}$$

where

$$\varepsilon(\mathbf{x}) = \begin{cases} \varepsilon_0, & \mathbf{x} \text{ belongs to the ventricles,} \\ 0, & \text{otherwise.} \end{cases}$$

The indicator function of the ventricles is found by the same procedure as the one used in Section II.B.1 for extracting the cortical mass function. Specifically, a threshold separating the ventricles from the surrounding tissues is selected interactively. A morphological erosion, followed by a 3D region growing, is then used to separate the ventricular regions. Finally, a morphological conditional dilation is used to recapture the ventricular regions. Finally, a morphological conditional dilation is used to recapture the ventricular volume eroded prior to region growing.

Having defined the ventricular strain, we now turn our attention to the elastic deformation of $\mathscr{V}_1$. Under linear elasticity, the Piola–Kirchhoff stress tensor is given by

$$\mathbf{S} = 2\lambda\mathbf{E} + \mu\, tr(\mathbf{E})\mathbf{I}, \tag{9}$$

and the equations governing the deformation of $\mathscr{V}_1$ are [28]

$$\mathbf{F} + \mathrm{Div}\mathbf{S} = 0. \tag{10}$$

Here, Div denotes the divergence of a tensor in the reference configuration, and $\mathbf{F}$ is the total external force field acting on $\mathscr{V}_1$ and is described later in this section.

In order to find Div$\mathbf{S}$ in our formulation, we use (9) and the fact that

$$\mathrm{Div}(\phi\mathbf{S}) = \phi\mathrm{Di}\mathbf{S} + \mathbf{S}\nabla\phi, \tag{11}$$

where $\phi$ is a scalar function and $\mathbf{S}$ is a tensor. Inserting (9) into (10), using (11), and after some algebra, we obtain the equilibrium equations

$$\begin{aligned} &\{\mathbf{F} + \lambda\Delta\mathbf{U} + (\lambda+\mu)\nabla\mathrm{Div}\mathbf{U}\} \\ &\quad + \{(\nabla\mathbf{U} + \nabla\mathbf{U}^{\mathrm{T}} - 2\mathbf{I})\nabla\lambda + (\mathrm{Div}\mathbf{U} - 3)\nabla\mu\} \\ &\quad + \{\varepsilon(2\nabla\lambda + 3\nabla\mu) + (2\lambda + 3\mu)\nabla\varepsilon\} = 0. \end{aligned} \tag{12}$$

The first term in (12) is identical to the left-hand side of the Navier equations [28], the second term results from

[2] The subscript $r$ is used here in order to distinguish the Lame moduli of this 2D reparameterizing transformation from those in the 3D warping transformation described in the following section.

[3] As customary in the continuum mechanics notation, we will omit the dependencies of the functions and the tensors on $\mathbf{x}$.

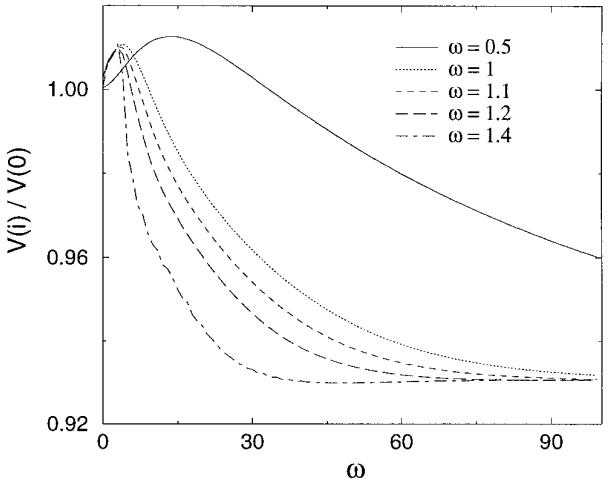


**FIG. 2.** The relative volumetric change of a selected brain region as a function of the iteration number, for different relaxation parameter ($\omega$) values.

the material inhomogeneity, and the third term results from the strain $\mathbf{E}_0$.

*Numerical Solution.* The equations in (12) are discretized and solved using successive overrelaxation [29]. As demonstrated in Fig. 2, overrelaxation increases the speed of convergence substantially, even in transformations of similar brains involving only small deformations. Specifically, Fig. 2 shows the convergence of the successive overrelaxation iterative procedure for different values of the relaxation parameter $\omega$. The measure plotted in Fig. 2 is the ratio of the volume of a selected region of the deformed brain at iteration $i$ over its volume in the undeformed brain; this region was far from the cortical and ventricular boundaries, and therefore convergence in this region was expected to be the slowest compared to other brain regions. The original and the target brains were purposely chosen to be very similar in this case, as shown by the small magnitude of deformation (7% volumetric change at convergence). This implies that the deformation is small and therefore the convergence is relatively fast. Even in this case, however, the rate of convergence is substantially increased with increasing $\omega$. We note, however, that for $\omega > 1.5$ we have noticed oscilatory behavior in certain cases. In our implementation we use $\omega = 1.4$.

*External Forces.* We now turn our attention to the external force field, $\mathbf{F}$, acting on the reference (undeformed) image. It is composed of two components. The first component is equal to

$$\mathbf{g}(\mathbf{x}) - \mathbf{U}(\mathbf{x}), \tag{13}$$

and it is applied to the outer cortical surface in $\mathcal{V}_1$ deforming it to its homologous surface in $\mathcal{V}_2$; this component favors 3D deformations which satisfy the outer cortical map $\chi$ in (6). The second component, denoted by $\mathbf{b}(\cdot)$, is a force field that is active in the interior of the brain and its purpose is to bring internal brain structures in better alignment. In our current formulation, $\mathbf{b}(\cdot)$ is applied to the ventricular boundaries, and it tends to align the ventricular boundaries of the deformed $\mathcal{V}_1$ image and the target image $\mathcal{V}_2$. Specifically, the force applied to a point $\mathbf{x}$ on the ventricular boundary in $\mathcal{V}_1$ is equal to (see Fig. 3)

$$\mathbf{b}(\mathbf{U}(\mathbf{x})) = w(\mathbf{U}(\mathbf{x}))\,[\mathbf{c}_v(\mathbf{U}(\mathbf{x})) - \mathbf{U}(\mathbf{x})], \tag{14}$$

where $\mathbf{c}_v(\mathbf{U}(\mathbf{x}))$ is the center of the ventricular boundary mass in $\mathcal{V}_2$ included in the neighborhood of the point $\mathbf{U}(\mathbf{x})$. The weight $w(\cdot)$ measures the coorientation of the deformed and the target ventricular boundaries; boundaries that are similarly oriented tend to be attracted more strongly to each other. Specifically, $w(\cdot)$ is given by

$$w(\mathbf{U}(\mathbf{x})) = \langle \mathbf{N}_1(\mathbf{U}(\mathbf{x})), \mathbf{N}_2(\mathbf{U}(\mathbf{x})) \rangle,$$

on the ventricular boundaries in $\mathcal{V}_1$ and zero elsewhere. Here, $\mathbf{N}_1(\cdot)$ is the outward normal along the ventricular boundary of the deformed reference image $\mathcal{V}_1$ and $\mathbf{N}_2(\cdot)$ is the outward normal of the ventricular boundary of $\mathcal{V}_2$. Since $\mathbf{N}_1(\cdot)$ is defined in the undeformed (reference) configuration, it is mapped to the deformed (spatial) configuration through the gradient of the vector field $\mathbf{U}(\cdot)$ (see [28]). The radius of the neighborhood in (14) is determined by adaptively growing a spherical neighborhood around a point on the ventricular boundary of the deformed reference image until it encompasses enough ventricular boundary points of the target image.

The ventricular force $\mathbf{b}(\cdot)$ in (14) vanishes when the two ventricular boundaries are coincident, and therefore it tends to bring them into alignment. The surrounding

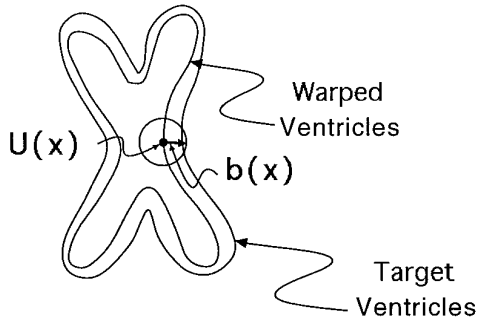


**FIG. 3.** The ventricular force tends to align the warped and the target ventricular boundaries.

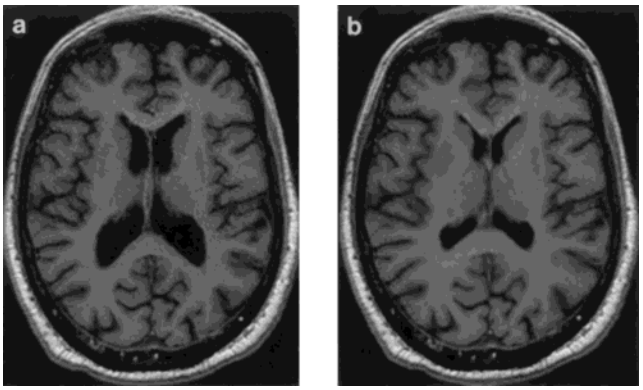


**FIG. 4.** An MR image from an individual with relatively large ventricles (a) and its transformation after applying a uniform stress within the ventricles (b).

structures are rearranged through the elastic forces within the brain.

*Material Inhomogeneity.* We have adopted the use of inhomogeneous elastic material primarily because different brain structures tend to have different variability. Accordingly, more variable structures should be allowed to deform more freely than less variable ones. In particular, the ventricles are highly variable across individuals, and especially across different ages. Therefore, they should have high flexibility to adapt their shape. In contrast, the subcortical structures tend to have much more consistent shape. Finally, the cortical folds can vary dramatically across individuals and should be flexible enough to deform freely; an example of the importance of material inhomogeneity in highly nonlinear transformations of the cortical folds is presented in Section III.E.

*Ventricular Strain.* The ventricular forces in Fig. 3 align the ventricular boundaries, provided that they are in proximity to each other. This is not always the case, however, especially in elderly or diseased brains in which often dramatic ventricular enlargements are present, which result in ventricular boundaries that are not sufficiently close to be attracted to each other. The uniform strain $\mathbf{E}_0$ accounts for such gross morphological irregularities, by expanding or contracting the ventricles in $\mathcal{V}_1$, and bringing them into rough alignment with the ventricles in $\mathcal{V}_2$. This is demonstrated in Fig. 4.

The degree of volumetric change imposed by a uniform strain depends, in general, on the shape of the ventricles and on their volume relative to the brain tissue. However, we have determined experimentally from images with a wide variety of ventricular sizes and shapes that the volumetric change is approximately a linear function of $\varepsilon_0$, as shown in Fig. 5. Based on this relationship and on the ratio of ventricular volumes of the reference and target images we determine the appropriate strain magnitude $\varepsilon_0$.

The framework of prestrained elasticity can also model other structural irregularities, besides ventricular expansion. In particular, in Section III.F we use it to simulate the growth of tumors and the deformation of their surrounding structures.

## III. EXPERIMENTS

### III.A. *Nearly Homothetic Map*

In our first experiment we test our hypothesis that the nearly homothetic map found through the iterative procedure of Section II.B.2 provides a rough correspondence between cortical regions in different brains. In this experiment we randomly selected six MR volumetric images and applied the procedures of Sections II.B.1 and II.B.2. A 3D rendering, viewed from the bottom and the top, of the resulting surfaces is shown in Fig. 6. Corresponding regions in the surfaces in Fig. 6 are found using the grid shown superimposed on the surfaces. A subset of the grid lines has been assigned letters so that the reader can identify individual corresponding points.

Figure 6 shows that the nearly homothetic map results in a good correspondence of the cortical regions. Landmarks such as the interhemispherical fissure, the anterior-most part of the frontal lobe, the occipital poles, the bottom part of the temporal lobes, the central sulcus and adjacent gyri, the superior frontal sulcus, and others fall in consistent locations in the grid.

### III.B. *Elastic Warping*

In our second experiment we tested the performance of the STAR algorithm by registering two MR volumetric

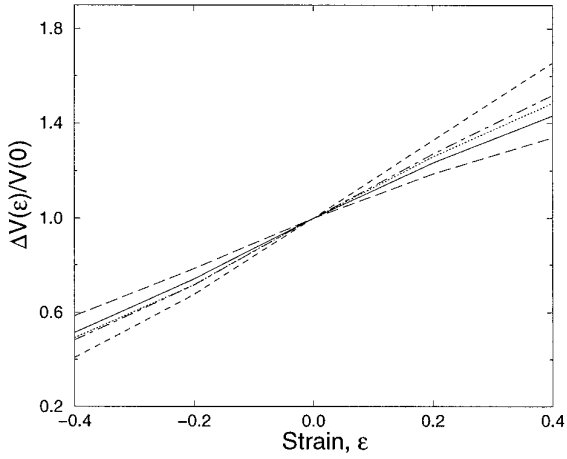


**FIG. 5.** The volumetric change resulting from a uniform strain of magnitude $\varepsilon$ in the ventricles, for five randomly selected images with a variety of ventricular sizes and shapes.

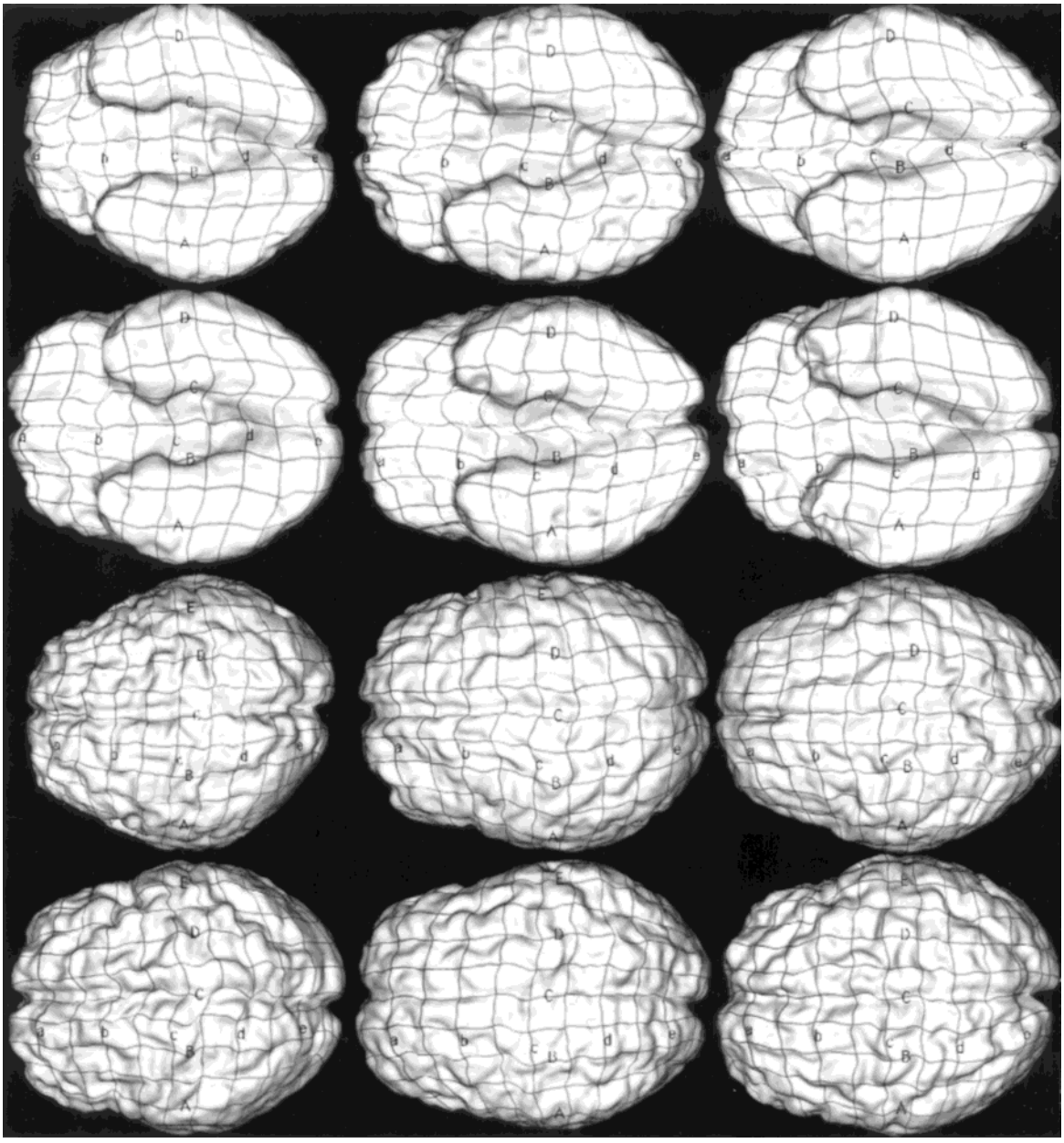

**FIG. 6.** The result of the deformable surface algorithm applied to six randomly selected individuals, viewed from the bottom and from the top. The superimposed labeled grid shows that regions that correspond to each other according to the nearly homothetic map described in Section II.B.2.

images. One of the images was taken from an elderly individual with relatively larger ventricles. We applied the deformable surface algorithm obtaining a map from the outer cortex of the individual with the smaller ventricles to the one with the larger ventricles (target dataset). We then applied the elastic warping procedure using the external force field of (13) and (14). The result is shown in Fig. 7, in which four different cross-sections of the original image, of the warped image, and of the target image are shown superimposed on the cortical and ventricular outlines of the target image. Notable is the good registration in the periventricular region, despite the difference in the ventricular size.

In Fig. 8 we show several of a total of 36 landmarks used to measure the registration accuracy in this experiment. The registration error at each landmark was the distance between the location of the landmark in the deformed image and its location in the target image. The landmarks are represented by crosses, the size of each being proportional to the registration error at that location. Interesting is the last cross-sectional image showing the two landmarks located at the depth of the central sulcus. The error was

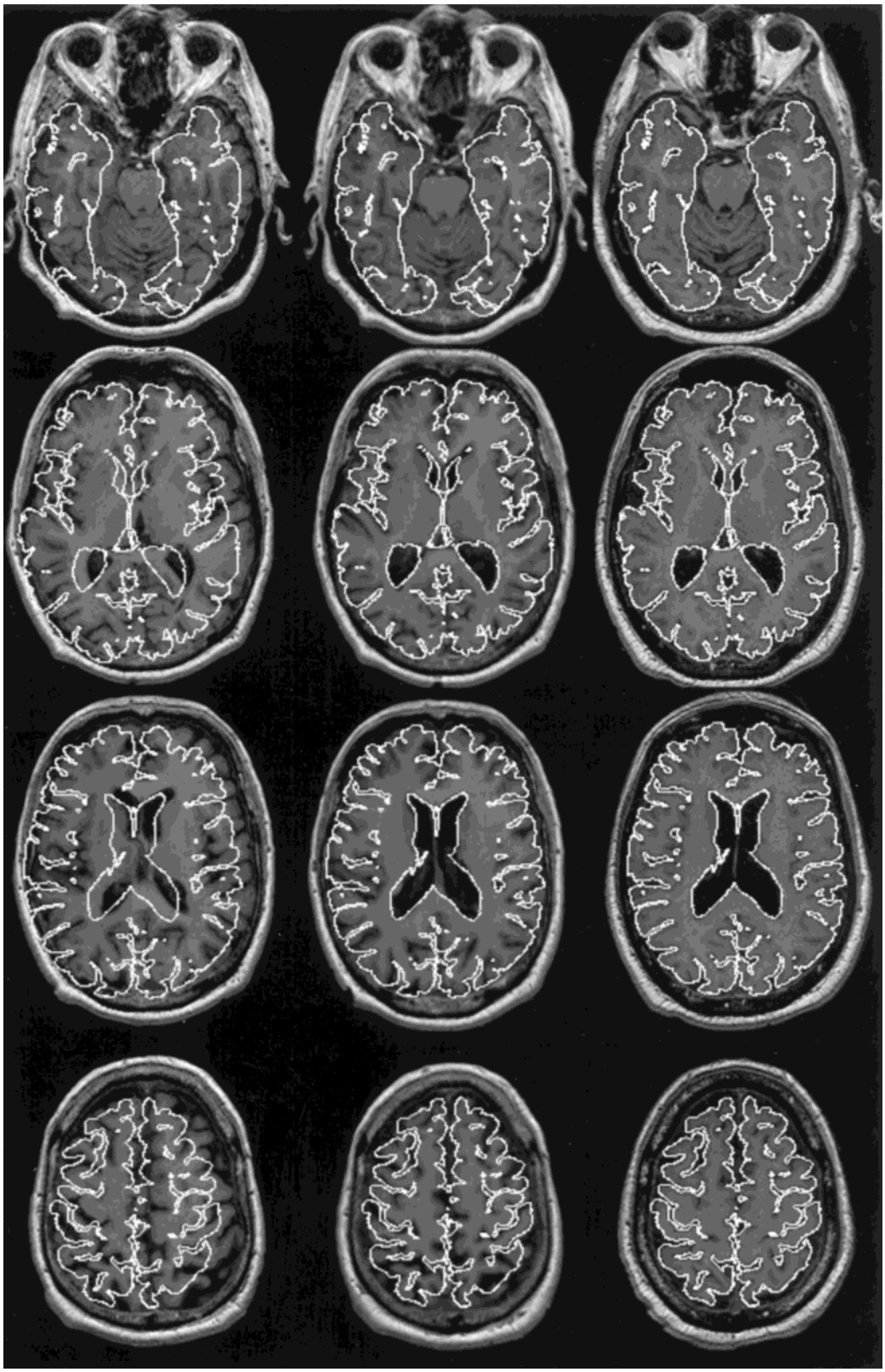

**FIG. 7.** Cross-sections from four different levels of the brain. On the left the cross-sections of the unwarped image are shown superimposed on the cortical and ventricular outlines of the target image and in the middle the cross-sections of the warped image are shown superimposed on the same outlines. For comparison purposes, on the right the same outlines are shown superimposed on the cross-sections of the target image, from which they were extracted. The similarity between the deformed (center) and the target (right) images reveals the good registration obtained through the STAR algorithm.

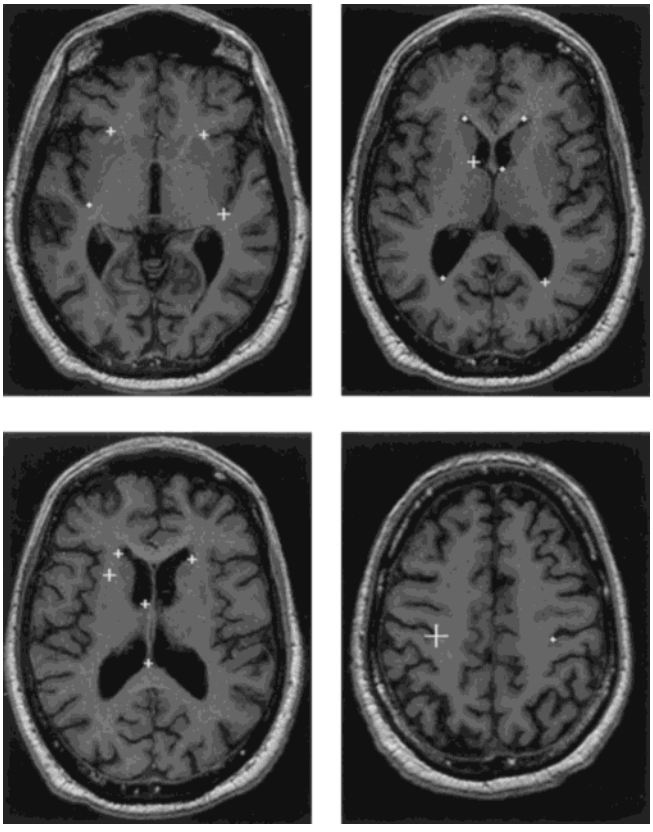

FIG. 8. Four representative cross-sections containing several of the 36 landmarks used to calculate the registration accuracy for the experiment of Fig. 7. The sizes of the crosses are proportional to the corresponding registation error at each landmark.

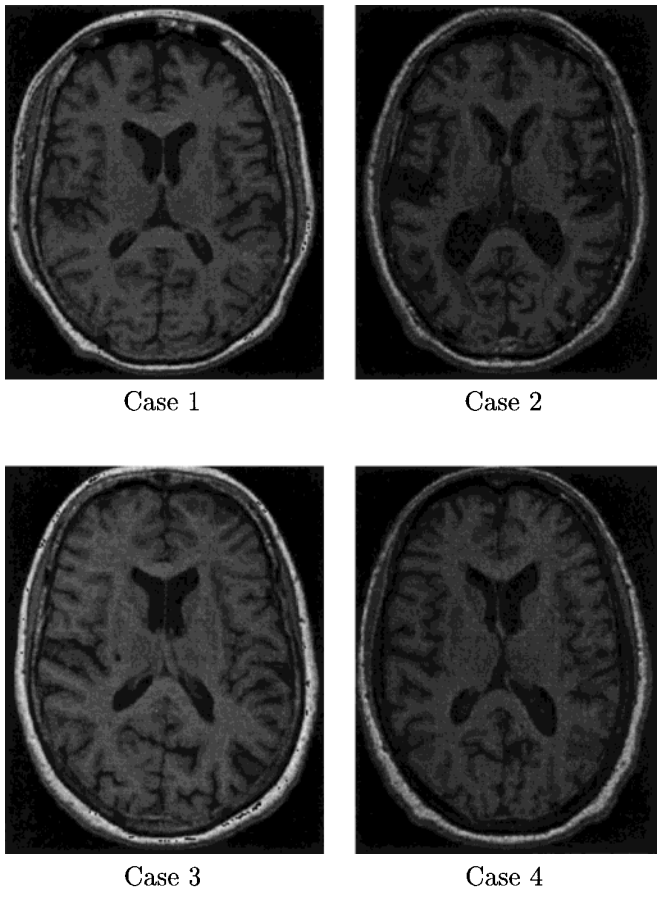


FIG. 9. A typical cross-section taken from the volumetric images of four of the five subjects in the experiments in Section III.B, showing the considerable differences in the size of the ventricles.

much larger on the left than on the right. This is due to the fact that no deep cortical features are used in our formulation in finding the registration transformation. Finding such features, and utilizing them in obtaining a more accurate transformation deep in the cortex, is a main direction of research in our laboratory [23, 30].

We subsequently obtained a quantitative measure of the performance of the STAR algorithm on five volumetric magnetic resonance images, with highly variable ventricular sizes. One typical cross-section from the 3D images is shown in Fig. 9 for each of the cases (Case 5 is the one shown in Fig. 7). We then applied the STAR algorithm, transforming these images toward a target image with relatively small ventricles. In these experiments the curvature-based matching was performed only in the coarse scale through the automated procedure described in Section II.B.3; no manual outline of cortical features was performed. We then selected a total of 90 cortical landmarks (on the average 22.5 per case) and 69 subcortical landmarks (on the average 17.25 per case) and measured the registration error. The mean, standard deviation, and maximum errors are shown in Table 1 for the cortical landmarks and in Table 2 for the subcortical landmarks. The average total time required for finding the 3D transformation was about 6 minutes per case.

In the experiments above, the values of the Lame moduli within the ventricles were smaller than their values in the brain. The exact ratio of these elastic parameters within the brain parenchyma over their values in the ventricles can be within a fairly wide range. In practice we typically set this ratio to 4, which allows for adequate ventricular

**TABLE 1**
**Registration Error on Cortical Landmarks**

| | Mean (mm) | Standard deviation (mm) | Maximum (mm) |
|---|---|---|---|
| Case 1 | 2.7 | 1.3 | 5.9 |
| Case 2 | 3.5 | 1.6 | 6.9 |
| Case 3 | 3.8 | 2.1 | 9.1 |
| Case 4 | 4.4 | 3.0 | 9.6 |
| Case 5 | 2.8 | 2.3 | 10.4 |
| Total | 3.4 | 2.1 | 10.4 |

**TABLE 2**
**Registration Error on Subcortical Landmarks**

| | Mean (mm) | Standard deviation (mm) | Maximum (mm) |
|---|---|---|---|
| Case 1 | 4.2 | 1.6 | 7.1 |
| Case 2 | 3.1 | 2.1 | 8.5 |
| Case 3 | 2.2 | 1.0 | 3.9 |
| Case 4 | 2.4 | 1.0 | 4.4 |
| Case 5 | 1.3 | 0.8 | 3.5 |
| Total | 2.5 | 1.6 | 8.5 |

flexibility, while maintaining the smoothness of the transformation within the ventricles. Overly small values of $\lambda$, $\mu$ can result in a transformation having a negative determinant.

### III.C. *Manual Matching of the Sulci*

In our third experiment we tested the procedure for curvature-based matching of individual sulci at the fine scale, which was described in Section II.B.3. In this experiment we registered two MR volumetric images, by first using only the nearly homothetic map between the outer cortical surfaces in the two images (see Section II.B.2). A cross-section of the warped MR image, from a level showing the central sulcus, is shown superimposed on the cortical outline of the target MR image in Fig. 10a. Although a good overall registration is apparent, the central sulcus and the adjacent gyri are mismatched by several millimeters (see arrows in Fig. 10a).

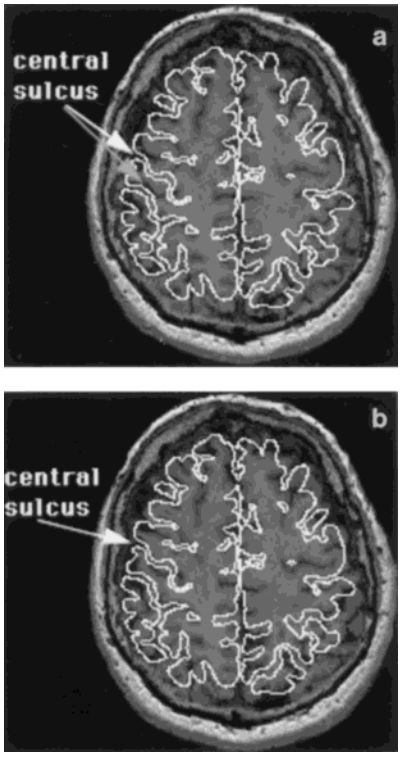


**FIG. 10.** A cross-section from the top of the brain including the central sulcus. The cross-section in (a) is from the warped MR image using only homothetic mapping. The cross-section in (b) is from the warped image using homothetic mapping followed by curvature-based matching of the central sulcus and the interhemispherical fissure. A considerable improvement in the region around the central sulcus is apparent. Note that besides the central sulcus, the pre- and postcentral sulci and adjacent gyri are also aligned much better in (b) than in (a).

We next calculated the minimum curvature along the outer cortex of each of the two images, which we show in Figs. 11a and 11b superimposed on the parametric domain $\mathscr{D}$. In Figure 11, the top of the images corresponds to the anterior of the brain and the bottom to the posterior. Based on these curvature maps, and assisted by the 3D rendering of the curvature superimposed on the nonflattened cortex, shown in Fig. 12, we outlined the central sulcus and the interhemispherical fissure. The outlined sulci are readily mapped on the outer cortical surface through the parameterization $\mathbf{x}(u, v)$ of each surface and are shown in Fig. 13. We then elastically deformed the parametric domain $\mathscr{D}$ in Fig. 11a by matching the outlined central sulcus and interhemispherical fissure, as described in Section II.B.3 ($N = 3$ in (4)). The deformed curvature map in shown in Fig. 11c. A better agreement between the curvatures in Figs. 11b and 11c is apparent, especially around the central sulcus and the interhemispherical fissure (the thick vertically oriented bright curve in the images in Fig. 11). Rulers on the horizontal and vertical axes have been added to visually assist in the assessment of the registration of the three features used in this reparameterization.

Finally, using the reparameterized surface we applied our 3D elastic warping transforming the first dataset to the second (target) dataset. A cross-section of the resulting image, taken from the same level as in Fig. 10a, is shown in Fig. 10b. This figure shows a better match of the regions around the central sulcus. It is worth noting that not only the central sulcus, but the adjacent sulci and gyri are better matched in Fig. 10b. This is because the elastic warping of the curvature maps allowed the sulci and gyri neighboring the central sulcus to ''slide'' along the outer cortical surface and match their counterparts in the target image.

### III.D. *Automatic Curvature-Based Matching*

In our fourth experiment we show results from our procedure for automatic curvature-based reparameterization of the outer cortical surface at the coarse scale. In this experiment we randomly selected two MR volumetric images, we applied the deformable surface algorithm, and we calculated the minimum and the maximum curvatures at coarse scale (the deformable surface was sampled with 5000 polygons). The top row in Fig. 14 shows the maximum

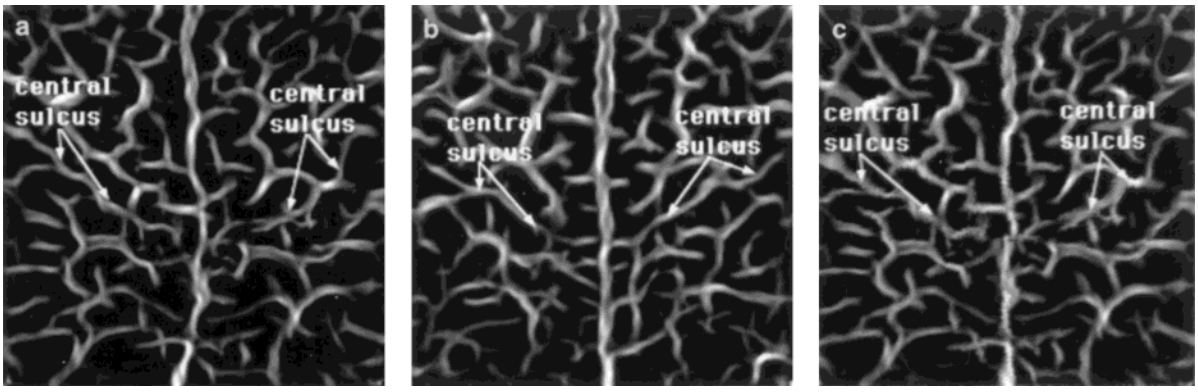


**FIG. 11.** The curvature maps of the outer cortex (the minimum curvature superimposed on the flattened outer cortical surface) for (a) the first and (b) the second (target) image used in the experiment in Section III.C. In (c) we show the elastically warped map in (a) obtained by matching the central sulcus and the interhemispherical line (shown as thick vertically oriented curve in all images). A better agreement of the curvatures in (c) and (b) is apparent, compared to that between (a) and (b).

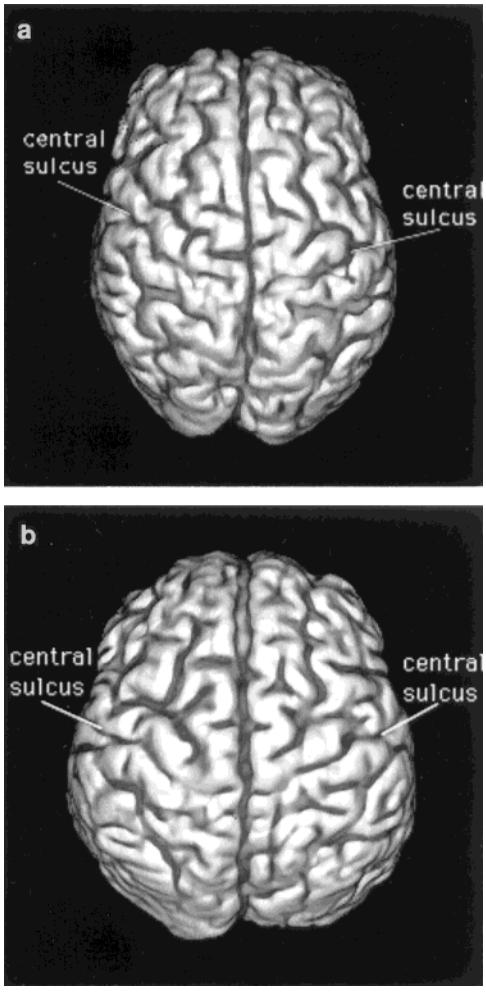


**FIG. 12.** The minimum curvature of the outer cortex shown (dark) superimposed on the outer cortex: (a) corresponds to the map in Fig. 11a and (b) corresponds to the map in Fig. 11b.

curvature for the bottom half of the cortex (left), and the minimum curvature for the bottom half (middle) and top half (right) of the cortex, for the target image (the top of the images corresponds to the anterior of the cortex and the bottom to the posterior). The analogous curvatures for the second (to be deformed) image are shown in the bottom row. For clarity, two of these curvatures are also shown in Fig. 15 superimposed on the rendered surfaces; the darker a region in Fig. 15 is, the higher its curvature (in absolute value) is. That is, dark regions in Fig. 15 correspond to bright regions in Fig. 14.

The maximum curvature reflects the shape of the ''rim'' formed by the bottom parts of the temporal and occipital lobes and the anterior part of the frontal lobes (left column in Fig. 14 and dark region in Fig. 15a). The minimum curvature of the top half shows the interhemispherical fissure (bright vertically oriented curve in Fig. 14, right column) and the minimum curvature of the bottom shows the gap between the left and right temporal lobes where the cerebelum is located (bright vertically oriented region in Fig. 14, middle column) and the anterior edge of the Sylvian fissure for the two hemispheres (the two horizontally oriented bright curves, middle column, in Fig. 14).

These curvatures were used to find a reparameterization, $\mathbf{r}(u, v)$, according to the procedure described in Section II.B.3. The curvatures of the reparameterized surface corresponding to the bottom row are shown in the middle row of Fig. 14. It is arrarent that the shapes of the curvatures shown in the middle row have now adapted to better match those of the top row. Notable is the adaptation of the posterior part of the interhemispherical fissure (bottom part of the bright region in the middle and right images, middle row). We note that each pixel of the low resolution images in Fig. 14 corresponds to one polygon of the deformable surface, which spans several millimiters in real space. Therefore, the seemingly small improvement in the

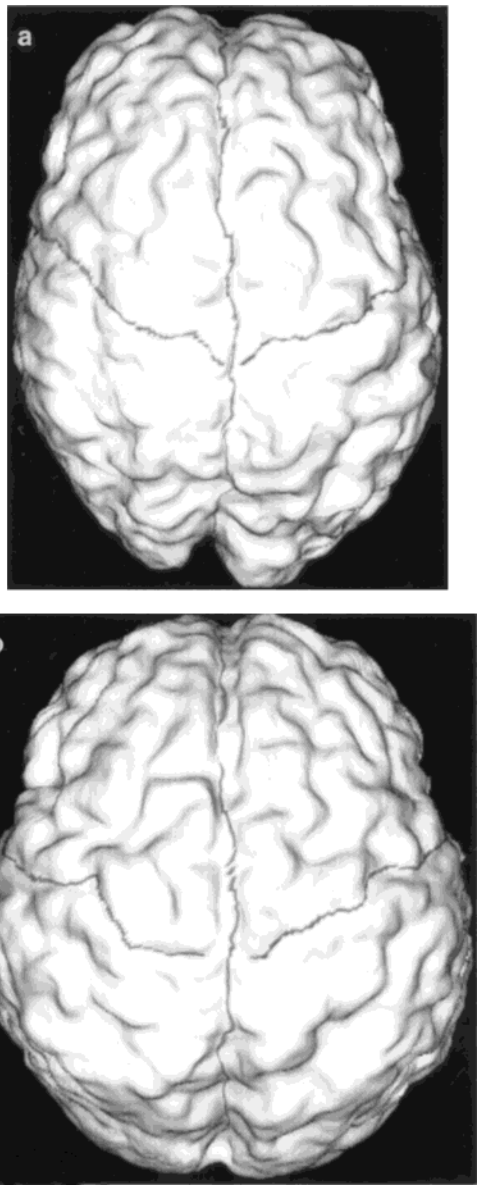


**FIG. 13.** The outlined central sulci and interhemispheric fissure (see Fig. 11) mapped on the outer cortical surface.

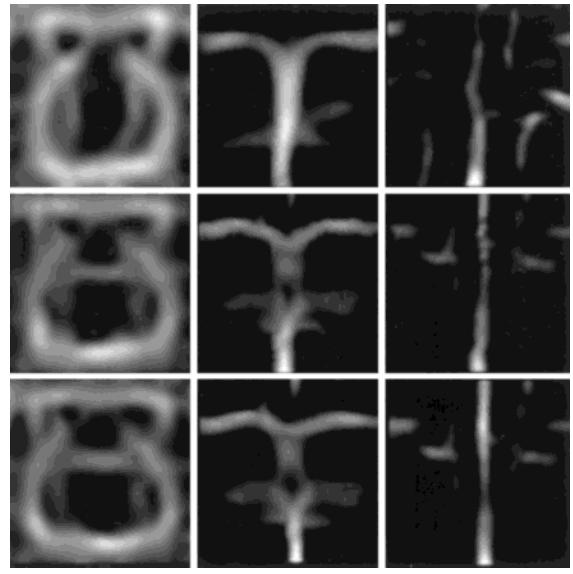

**FIG. 14.** Top and bottom rows: Minimum and maximum curvatures of the outer cortex from two volumetric images. Middle row, the same curvatures of the reparameterized surface corresponding to the bottom row. A better agreement between the curvatures in the middle and top rows is apparent, compared to that between the top and the bottom rows.

similarity of the curvatures in Fig. 14 is actually very important because it translates to a registration improvement of several millimeters.

### III.E. *Material Inhomogeneity*

In our experiments up to now in this section we have used different elastic properties within the ventricles ($\lambda$ and $\mu$ in the ventricles were one quarter of their value in the brain), which has allowed them to expand or contract more freely. In our previous experiment we demonstrate the importance of material inhomogeneity in the registration of the highly variable cortical folds. In particular, we created two synthetic images (see Figs. 16a and 16b), which are identical except for the difference in the orientation of the two folds. We warped Figs. 16a to 16b using a homogeneous elastic material throughout the brain, and we obtained the result shown in Fig. 16c. We then warped Fig. 16a to Fig. 16b using an inhomogeneous elastic material and obtained the result shown in Fig. 16d. The apparent stretching of the cortex in Fig. 16c was eliminated in Fig. 16d by using a more flexible elastic material in the white region, which allowed the folds to deform more freely.

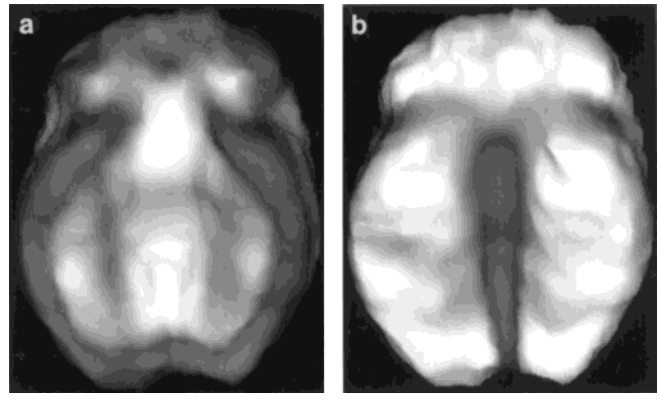


**FIG. 15.** A rendering of the coarse representation of the outer brain boundary, with the maximum and the minimum curvatures shown darker. The curvature in (a) corresponds to the bottom left image in Fig. 14 and the curvature in (b) corresponds to the bottom middle image in Fig. 14.

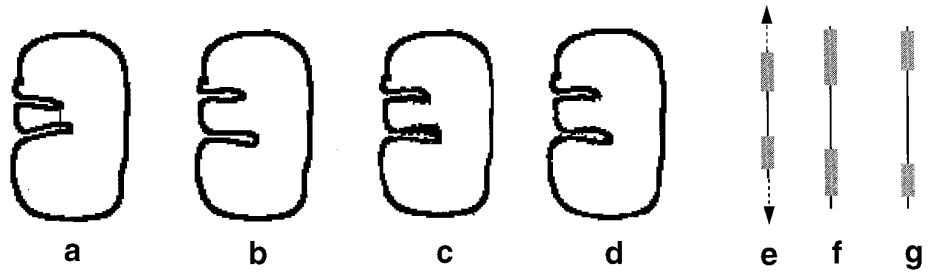


**FIG. 16.** A demonstration of the effect of material inhomogeneity. (a) and (b) Two synthetic images. (c) and (d) The elastic warping of (a) toward (b) using homogeneous material (c), and inhomogeneous material (d) with higher flexibility (smaller $\lambda$, $\mu$) in the white region. The reason for the improvement obtained using inhomogeneous elastic media is shown schematically in (e), (f), and (g). (e) A cross-section shown as a vertical black segment in (a), in which the gray corresponds to the cortex (black in (a)), and the rest corresponds to the white in (a). The two endpoints of this elastic vertical cross-section were stretched in (f), representing the stretch imposed by matching the two cortical folds in (a) and (b), assuming homogeneous media. Because of the media homogeneity, the deformation was absorbed evenly by the gray and black regions in (f). However, if an inhomogeneous media with ratio of Lame moduli equal to 10 is used, the deformation is absorbed mostly by themore flexible material (g).

The effect of material inhomogeneity is illustrated in more detail in Figs. 16e–16g. Specifically, Fig. 16e schematically shows a cross-section corresponding to the vertical line segment in Fig. 16 spanning the region between the two folds (the gray regions in Fig. 16e correspond to cross-sections of the two folds in Fig. 16a). Figure 16f show the effect of a stretching of this section when it is pulled from its two endpoints, assuming that the elastic material along this section is homogeneous. The stretching in Fig. 16f has been absorbed evenly by the folds and the in-between region. However, if a 10 times more flexible material is used between the folds, it will absorb virtually all of the deformation, as shown in Fig. 16g, maintaining the thickness of the folds and therefore resulting in more realistic deformations.

### III.F. *Tumor Growth*

In our experiments up to now we have demonstrated the use of the framework of prestrained elasticity in modeling the ventricular expansion occurring with aging. The same framework can be utilized in modeling other structural changes in the brain and in particular the growth of tumors and the deformation of the surrounding structures. Figure 17a shows a cross-sectional magnetic resonance image of the brain and Fig. 17b shows the same image with the initial shape of a (hypothetical) tumor. Figure 17c shows the resulting tumor after the growth induced by a strain energy uniformly distributed within the tumor in Fig. 17b.

## IV. SUMMARY AND CONCLUSIONS

We have presented a new technique for the spatial transformation of brain images. Our methodology is based on a surface-to-surface mapping between two images to be registered, which is used to drive a three-dimensional elastic warping of the images. An internal force applied to the ventricular boundaries brings the ventricles and the surrounding structures in better correspondence. The spatially varying elasticity allows certain structures, such as

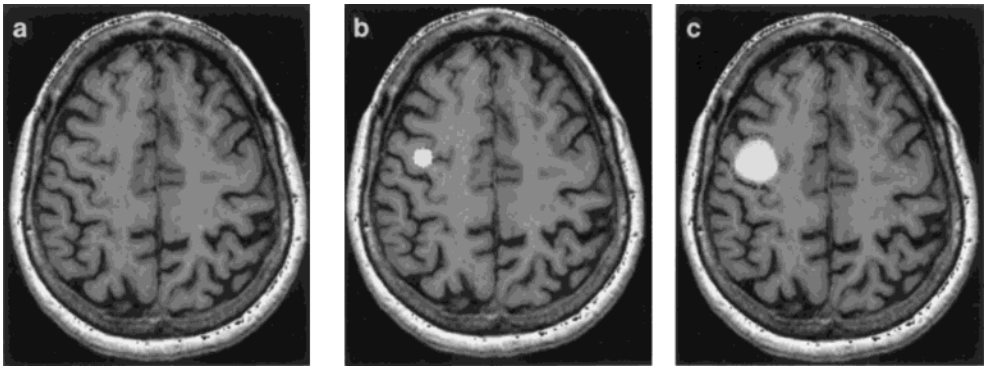


**FIG. 17.** The use of prestrained elasticity in modeling tumor growth. (a) A cross-section from a volumetric MR image. (b) A cross-section from an initial (hypothetical) spherical tumor placed in (a). (c) A cross-section from the resulting expanded tumor.

the ventricles, to deform more freely than others. Finally, a uniform strain applied to the ventricles causes their expansion, allowing the external forces to better align the ventricular boundaries.

The STAR algorithm was tested by registering MR images. In particular, we showed that homothetic mapping, which consists of a uniform stretching or shrinking followed by an arbitrary bending, brings cortical regions in an overall good correspondence. We obtained such a map by using a deformable surface algorithm, which yields a mathematical representation of the outer cortical surface. We used the correspondence determined by homothetic mapping to elastically warp images into register with each other.

Despite the overall good registration obtained using homothetic mapping, there is still a considerable registration error, which is largely due to anatomical variability in individual brain features. Specifically, although homothetic mapping accounts for an arbitrary bending of the brain boundary, it allows only a uniform expansion or contraction of the outer cortical surface. Equivalently, it accounts for any overall shape differences of the brain but it assumes that an observer sitting on the outer cortical surface sees the same cortical folding pattern in all individuals. This assumption is the main limitation of homothetic mapping, given the intersubject variability of the cortical folding pattern.

To overcome this limitation we used a procedure which refines the homothetic map, and allows a nonuniform stretching or shrinking of the outer cortical surface by matching features identified through the curvature maps. By using the resulting map in our 3D elastic warping, we demonstrated a considerable improvement in the registration accuracy in the neighborhood of the features used. Most notable was the improvement in the registration around the central sulcus (improvement of $\sim$5 mm). The nonuniform mapping allowed the central sulcus and the neighboring sulci and gyri to slide along the outer cortical surface and match their counterparts in the target image.

Several extensions of our basic technique are possible. In particular, in this paper we focused on the alignment of the outer cortical and the ventricular boundaries. In addition to these surfaces, internal cortical features, such as the deep sulcal surfaces, can be used for matching of the internal structures of the cortex. Current research in our laboratory in that direction focuses on the modeling the deep sulcal surfaces as ribbons, which can be matched based on their differential geometric properties and are reported in a separate paper [23, 30].

Extensions to our procedure for sulcal matching are also possible. In particular, a main focus of our current and future research is the development of an automatic sulcal identification and matching technique, assisted by prior probability distrubutions reflecting our expectation about the location and shape of the cortical folds.

Finally, the framework of prestrained elasticity for modeling tumor growth must be extended to allow for large deformations. In particular, our current formulation is based on linear elasticity which assumes a small deformation between the reference and the deformed images. In modelling tumor growth, this is not the case, and therefore nonlinear elasticity must be used.

## ACKNOWLEDGMENTS

The author thanks Nick Bryan for his support to this work. This work was partially supported by a Whitaker Biomedical Research Grant and by the NIH Grants NHI-AC-93-07 and 1R01 AG13743-01.

## REFERENCES

1. K. J. Friston, A. P. Holmes, K. J. Worsley, J. P. Poline, C. D. Frith, and R. S. J. Frackowiak, Statistical parametric maps in functional imaging: A general linear approach, *Hum. Brain Mapping,* 1995, 189–210.
2. A. C. Evans, *et al.*, Anatomical mapping of functional activation in stereotactic coordinate space. *Neuroimage,* **1,** 1992, 43–53.
3. C. Davatzikos, M. Vaillant, S. Resnick, J. L. Prince, S. Letovsky, and R. N. Bryan, A computerized approach for morphological analysis of the corpus callosum, *J. Comput. Assist. Tomogr.* **20,** 1996, 88–97.
4. G. Subsol, J. P. Thirion, and N. Ayache, Application of an automatically built 3D morphometric brain atlas: Study of cerebral ventricle shape, in *Visualization in Biomedical Computing,* Lecture Notes in Computer Science, 1996, pp. 373–382.
5. G. Subsol, J. P. Thirion, and N. Ayache, A general scheme for automatically building 3D morphometric anatomical atlases: Application to a skull atlas, INRIA Technical Report 2586, 1995.
6. F. L. Bookstein, Principal warps: Thin-plate splines and the decomposition of deformations, *IEEE Trans. Pattern Anal. Mach. Intell.* **11**(6), 1989, 567–585.
7. F. L. Bookstein, Thin-plate splines and the altas problem for biomedical images, in *Proceedings of the 12th International Conference on Information Processing in Medical Imaging, 1991,* pp. 326–342.
8. J. C. Gee, M. Reivich, and R. Bajcsy. Elastically deforming 3D atlas to match anatomical brain images, *J. Comput. Assist. Tomogr.* **17,** 1993, 225–236.
9. R. Bajcsy and S. Kovacic, Multiresolution elastic matching, *Comput. Vision Graphics Image Process.* **46,** 1989, 1–21.
10. C. Broit, *Optimal Registration of Deformed Images,* Ph.D. thesis, University of Pennsylvania, 1981.
11 M. I. Miller, G. E. Christensen, Y. Amit, and U. Grenander. Mathematical textbook of deformable neuroanatomies, *Proc. Nat. Acad. Sci.* **90,** 1993, 11944–11948.
12. G. E. Christenesen, R. D. Rabitt, and M. I. Miller. A deformable neuroanatomy textbook based on viscous fluid mechanics, in *Proceedings of 27th Annual Conference on Information Sciences and Systems, 1993,* pp. 211–216.
13. D. L. Collins, P. Neelin, T. M. Peters, and A. C. Evans, Automatic 3D intersubject registration of MR volumetric data in standardized Talairach space, *J. Comput. Assist. Tomogr.* **18,** 1994, 192–205.
14. J. Declerck, G. Subsol, J. P. Thirion, and N. Ayache, Automatic retrieval of anatomical structures in 3D images, in *Proceedings of the Conference on Computer Vision, Virtual Reality, and Robotics in Medicine, 1995,* pp. 153–162.

15. K. J. Friston, J. Ashburner, C. D. Frith, J. B. Poline, J. D. Heather, and R. S. J. Frackowiak, Spatial registration and normalization of images, *Hum. Brain Mapping* **2,** 1995, 165–189.
16. J. P. Thirion, Fast intensity-based non-rigid matching, in *Proceedings of 2nd International Symposium on Medical Robotics and Computer Assisted Surgery, 1995,* pp. 47–54.
17. J. Park, D. Metaxas, and L. Acel, Analysis of left ventricular wall motion based on volumetric deformable models and MRI-SPAMM, *Med. Image Anal.* **1,** 1996, 53–71.
18. J. Declerck, J. Feldmar, and F. Betting. Automatic registration and alignment on a template of cardiac stress and rest SPECT images, in *Proceedings, IEEE Workshop on Mathematical Methods on Biomedical Image Analysis. 1996,* pp. 212–221.
19. A. A. Amini, R. L. Owen, P. Anadan, and J. S. Duncan, Non-rigid motion estimation models for tracking the left ventricular wall, *Inform. Process. Med. Imag.* 1991, 343–357.
20. T. S. Denney Jr. and J. L. Prince, Reconstruction of 3D left ventricular motion from planar tagged cardiac MR images: An estimation theoretic approach, *IEEE Trans. Med. Imaging* **4,** 1995, 625–635.
21. C. Kambhamettu and D. B. Goldgov, Curvature-based approach to point correspondence recovery in conformal nonrigid motion, *CVGIP: Image Understanding* **60,** 1994, 26–43.
22. A. A. Young, D. L. Kraitchman, and L. Axel, Deformable models for tagged MR images: Reconstruction of two- and three-dimensional heart wall motion, in *Proceedings of the IEEE Workship on Biomedical Image Analysis, 1994.*
23. M. Vaillant, C. Davatzikos, and R. N. Bryan, Finding 3D parametric representations of the deep cortical folds, in *Proceedings of the IEEE Workshop on Mathematical Methods in Biomedical Image Analysis, June 1996,* pp. 151–159.
24. C. Davatzikos and R. N. Bryan, Using a deformable surface model to obtain a shape representation of the cortex, *IEEE Trans. Med. Imaging* **15,** 1996, 785–795.
25. C. Davatzikos and R. N. Bryan, Using a deformable surface model to obtain a mathematical representation of the cortex, in *Proceedings of the IEEE Computer Vison Symposium, Nov. 1995,* pp. 212–217.
26. R. Millman and G. Parker, *Elements of Differential Geometry,* Prentice-Hall, Englewood Cliffs, New Jersey, 1977.
27. C. Davatzikos, J. L. Prince, and R. N. Bryan, Image registration based on boundary mapping, *IEEE Trans. Med. Imaging* **15**(1), 1996, 112–115.
28. M. E. Gurtin, *An Introduction to Continuum Mechanics,* Academic Press, Orlando, 1981.
29. G. H. Golub and C. F. Van Loan, *Matrix Computations,* Johns Hopkins Press, Baltimore, 1983.
30. M. Vaillant and C. Davatzikos, Finding parametric representations of the cortical sulci using an active contour model, in *Medical Image Analysis,* Oxford Univ. Press, to appear.